catalysts

MDPI

Article

$Ce_{1-x}Fe_xVO_4$ with Improved Activity for Catalytic Reduction of NO with NH_3

Li Wang [1], Junbo Wang [2], Heping Cheng [3,4], Xiangxiang Zhou [2] and Zhen Ma [5,6,*]

1 College of Biology and Environmental Engineering, Zhejiang Shuren University, Hangzhou 310015, China; wlll36@163.com
2 Key Laboratory of Inorganic Functional Materials, School of Chemistry and Chemical Engineering, Huangshan University, Huangshan 245041, China; wangjunbo@tech.hsu.edu.cn (J.W.); zxx169385@163.com (X.Z.)
3 School of Information Engineering, Huangshan University, Huangshan 245041, China; chenghp@tech.hsu.edu.cn
4 State Key Laboratory of Precision Spectroscopy, East China Normal University, Shanghai 200062, China
5 Department of Environmental Science and Engineering, Fudan University, Shanghai 200433, China
6 Shanghai Institute of Pollution Control and Ecological Security, Shanghai 200092, China
* Correspondence: zhenma@fudan.edu.cn

Abstract: A series of $Ce_{1-x}Fe_xVO_4$ (x = 0, 0.25, 0.50, 0.75, 1) catalysts prepared by modified hydrothermal synthesis were used for selective catalytic reduction (SCR) of NO_x with NH_3. Among them, $Ce_{0.5}Fe_{0.5}VO_4$ showed the highest catalytic activity. The catalysts were characterized by X-ray diffraction (XRD), N_2 adsorption–desorption, scanning electron microscopy (SEM), transmission electron microscopy (TEM), energy-dispersive X-ray spectroscopy (EDX), X-ray fluorescence (XRF), X-ray photoelectron spectroscopy (XPS), temperature-programmed reduction using H_2 (H_2-TPR), and temperature-programmed desorption of NH_3 (NH_3-TPD). The results indicated the formation of Ce-Fe-V-O solid solutions. The average oxidation states (AOS) of Ce, Fe, V, and O atoms changed obviously with the incorporation of Fe^{3+} into $CeVO_4$, and the acidity of $Ce_{0.5}Fe_{0.5}VO_4$ differs from that of $CeVO_4$ and $FeVO_4$. The presence of more acid sites and a sharp increase in active oxygen species in $Ce_{0.5}Fe_{0.5}VO_4$ effectively improved the selective catalytic reduction (SCR) activity.

Keywords: selective catalytic reduction; nitrogen oxides; cerium vanadate; iron vanadate; cerium-iron vanadate

Citation: Wang, L.; Wang, J.; Cheng, H.; Zhou, X.; Ma, Z. $Ce_{1-x}Fe_xVO_4$ with Improved Activity for Catalytic Reduction of NO with NH_3. *Catalysts* **2022**, *12*, 549. https://doi.org/10.3390/catal12050549

Academic Editor: Hamidreza Arandiyan

Received: 15 March 2022
Accepted: 11 May 2022
Published: 17 May 2022

1. Introduction

NO_x pollutants released from power plants and car emissions have attracted much concern for their serious harm to the atmospheric environments and human health. The selective catalytic reduction (SCR) of NO_x with NH_3 has been extensively studied as one of the most effective methods to remove NO_x [1–3]. V_2O_5-WO_3-TiO_2 is the most widely used SCR catalyst for its extraordinarily high activity in NO reduction. However, it generally operates in a high-temperature window (300–400 °C), and it can be deactivated by the flue gas containing H_2O/SO_2, phosphorus, ash, and alkali metals [4,5]. CeO_2-based materials have been studied as either catalysts or catalyst supports due to their excellent redox property and oxygen-storage capacity [6]. These catalysts include CeO_2-WO_3-TiO_2 [7], CeO_2-ZrO_2-WO_3 [8], Mn/Ce-ZrO_2 [9], MnO_x-CeO_2 [10], Sn-MnO_x-CeO_2 [11], MnO_x-CeO_2 [12], and V_2O_5/CeO_2 [13]. However, CeO_2-based catalysts may suffer from sulfation [14].

Metal vanadates (AVO_4, A = La, Fe, Ce, etc.) is another kind of catalysts attracting attention. The reported AVO_4-based catalysts include $FeVO_4/TiO_2$ [15], Ni-$FeVO_4/TiO_2$ [16], $Fe_xEr_{1-x}VO_4$ [17], Sn-$CeVO_4$ [18], Sb-$CeVO_4$ [19], $Ce_{0.5}RM_{0.5}VO_4$ (RM = Tb, Er, or Yb) [20], $LaVO_4/TiO_2$-WO_3-SiO_2 [21], $CeV_{1-x}W_xO_4$ [22], and Zr-$CeVO_4/TiO_2$ [23]. For instance, Zr-$CeVO_4/TiO_2$ has high N_2 selectivity and H_2O/SO_2 durability in NH_3-SCR [23]. However, further promotion of AVO_4 is needed [24,25].

Generally, there are two approaches to design better NH_3-SCR catalysts. One approach is to modify the primary catalyst with one metal oxide or multiple metal oxides. The other approach is to modify supports used to disperse transition metal oxides [26]. In particular, the formation of metal oxide solid solutions may lead to better catalytic properties [27], since it may increase the catalyst's surface area, thermal stability, and the number of active oxygen sites.

Previous research reported that Sn, Zr, La, etc., were doped into $CeVO_4$ [18,22,24,28] separately to investigate their influences on NO conversion. For instance, Huang et al. developed $Sn_{0.20}Ce_{0.80}VO_4$ for NH_3-SCR by citric-acid-assisted solvothermal synthesis and post-hydrothermal treatment [18]. Zhao et al. developed $Ce_{0.85}Zr_{0.15}VO_4$ for NH_3-SCR [24]. However, the content of Sn or Zr in the solid solutions was not very high. Kang et al. synthesized a series of $Fe_\delta Ce_{1-\delta}VO_4$ ($\delta \leq 0.4$) catalysts with good SO_2 tolerance and NO conversion activity by a hydrothermal method [14]. The highest NO conversion appeared at $\delta = 0.3$ for $Fe_\delta Ce_{1-\delta}VO_4$ ($\delta \leq 0.4$). When the Fe content was higher, minor segregation of CeO_2 occurred.

In this paper, $Ce_{1-x}Fe_xVO_4$ ($x \leq 0.75$) solid solutions were prepared by a modified sol-gel hydrothermal method. The objective of our research was to incorporate more Fe into the solid solution to increase the number of active oxygen sites, facilitate the interactions among Ce, Fe, and V in fully mixed solid solutions, and achieve high activity in NH_3-SCR.

2. Results and Discussion

2.1. Catalytic Performance

Figure 1 depicts the NO_x conversions on five catalysts, in the reaction temperature range of 150–400 °C. The NO_x conversion on these catalysts increases as the temperature increases from 150 to 300 °C, and then decreases. Among them, $Ce_{0.5}Fe_{0.5}O_4$ gives the highest NO_x conversion (75.3%) at 300 °C. The catalytic activities of $FeVO_4$ and $CeVO_4$ are lower than those of $Ce_{1-x}Fe_xVO_4$. The overall activity of these catalysts follows the trend of $CeVO_4 < Ce_{0.75}Fe_{0.25}VO_4 < Ce_{0.5}Fe_{0.5}VO_4 > Ce_{0.25}Fe_{0.75}VO_4 > FeVO_4$, and the catalytic data are reproducible (Figure S1 in Supplementary Materials). It should be mentioned that the objective of this research was to identify the activity trends among these catalysts, i.e., to identify the best catalyst and understand why it is better than other catalysts. In addition, a small catalyst weight (200 mg) and a high flow rate (1000 mL/min) were adopted herein. Thus, the highest conversion was not 100%. Nevertheless, complete conversion can usually be achieved easily when more catalyst is used or the flow rate of the gas is decreased [27].

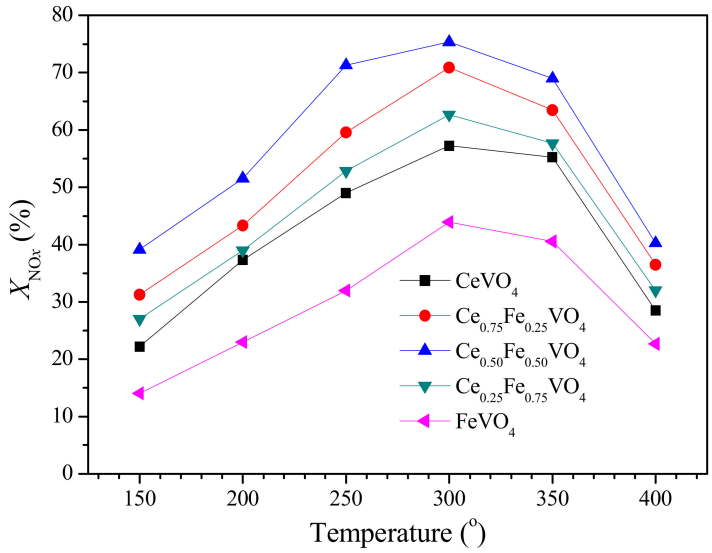

Figure 1. X_{NOx} over $Ce_{1-x}Fe_xVO_4$ catalysts prepared by a hydrothermal method. Reaction conditions: [NO] = 500 ppm, [NH_3] = 500 ppm, [O_2] = 3 vol.%, balance N_2; catalyst weight: 200 mg; total flow rate: 1000 mL·min^{-1}.

The stability of the optimal catalyst ($Ce_{0.5}Fe_{0.5}VO_4$) at 300 °C was tested as a function of time on stream. As shown in Figure S2 from Supplementary Materials, the NO_x conversion increases slightly in the initial 100 min, and it then becomes stable (74–75% conversion).

To set the result in perspective, the catalytic activity of $Ce_{0.5}Fe_{0.5}VO_4$ was compared with those of other catalysts. $Ce_{0.5}Fe_{0.5}VO_4$ is more active than $Ce_{0.5}Fe_{0.5}O_x$ reported in our previous work [27] because $Ce_{0.5}Fe_{0.5}O_x$ can only achieve about 70% NO_x conversion at 300 °C under relatively milder conditions (200 mg catalyst, [NO] = 500 ppm, flow rate = 500 mL/min) [27], whereas $Ce_{0.5}Fe_{0.5}VO_4$ can achieve 75.3% NO_x conversion at 300 °C under relatively harsher conditions (200 mg catalyst, [NO] = 500 ppm, flow rate = 1000 mL/min). For comparison, $Fe_{0.3}Ce_{0.7}VO_4$ developed by Zhang and co-workers can lead to >95% NO_x conversion at 250–300 °C under relatively milder conditions (300 mg catalyst, [NO] = 500 ppm, flow rate = 250 mL/min) [14]. In a recent work by Tang and co-workers, Ce-W/TiO_2 can leads to ~90% NO conversion at 300 °C under conditions identical to those in our current work (200 mg catalyst, [NO] = 500 ppm, flow rate = 1000 mL/min) [29].

2.2. Regular Characterization

Figure 2 gives the XRD patterns of samples. $CeVO_4$ shows peaks at 2θ = 18.4, 24.3, 32.7, 34.6, 39.3, 43.8, 48.2, and 55.9°, attributed to the (101), (200), (112), (220), (301), (103), (312), and (420) planes of tetragonal $CeVO_4$, respectively [30]. The other minor peaks are all consistent well with the standard pattern of $CeVO_4$ (JCPDS: 12-0757). The XRD patterns of $FeVO_4$ shows characteristic peaks at 25.2, 27.1, 27.8, 28.0, 42.1, 42.2, 49.8, 52.4, 54.8 and 59.2°, are ascribed to the (012), ($\bar{2}$01), (1$\bar{1}$2), ($\bar{2}$10), ($\bar{3}$10), (0$\bar{3}$3), (123), (3$\bar{1}$2), ($\bar{4}$12) and (2$\bar{2}$3) lattice planes of triclinic $FeVO_4$ (JCPDS: 71-1592) [31]. The XRD patterns of $Ce_{0.75}Fe_{0.25}VO_4$, $Ce_{0.5}Fe_{0.5}VO_4$, and $Ce_{0.25}Fe_{0.75}VO_4$ are similar to that of $CeVO_4$, indicating that the former samples keep the structure of $CeVO_4$.

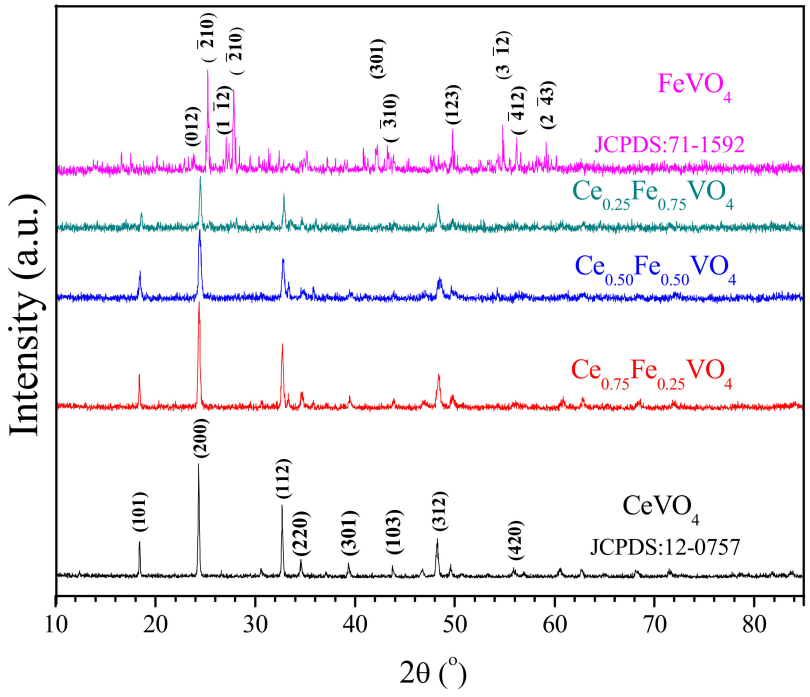

Figure 2. XRD patterns of $Ce_{1-x}Fe_xVO_4$ catalysts.

The magnified (200) peak of $CeVO_4$, $Ce_{0.75}Fe_{0.25}VO_4$, $Ce_{0.5}Fe_{0.5}VO_4$, and $Ce_{0.35}Fe_{0.75}VO_4$ are manifested in Figure S3 from Supplementary Materials. It is clear to see that the 2θ value right shifts to the lager value with the increase in Fe content, because the ion radius of the doped Fe^{3+} (49 pm) is much smaller than that of Ce^{3+} (103.8 pm) [32,33]. According to the Bragg's law, $2d_{(hkl)}\sin\theta = n\lambda$, the increase of 2θ value corresponds to the decrease

in the d spacing $d_{(hkl)}$ value, that is, lattice constraint. This fact implies that the Fe^{3+} ions substitute some Ce^{4+} sites. With the increase in Fe contents, the crystal parameter "a" gradually decreases from 0.7399 to 0.7349 nm, while the crystal parameter "c" gradually decreases from 6.496 to 6.469 nm (Table S1 in Supplementary Materials). Once the Fe^{3+} ions are doped into the crystal cell, the cell volume will shrink.

Figure 3 shows the SEM images of samples. The sizes of $CeVO_4$ crystals are a few-hundred nanometers, and $CeVO_4$ is composed of irregular particles, rods, and plates. The sizes of $FeVO_4$ crystals are also a few hundred nanometers, and $FeVO_4$ is composed of agglomerated particles. $Ce_{0.75}Fe_{0.25}VO_4$, $Ce_{0.50}Fe_{0.50}VO_4$, and $Ce_{0.25}Fe_{0.75}VO_4$ generally exhibit morphologies more similar to that of $CeVO_4$.

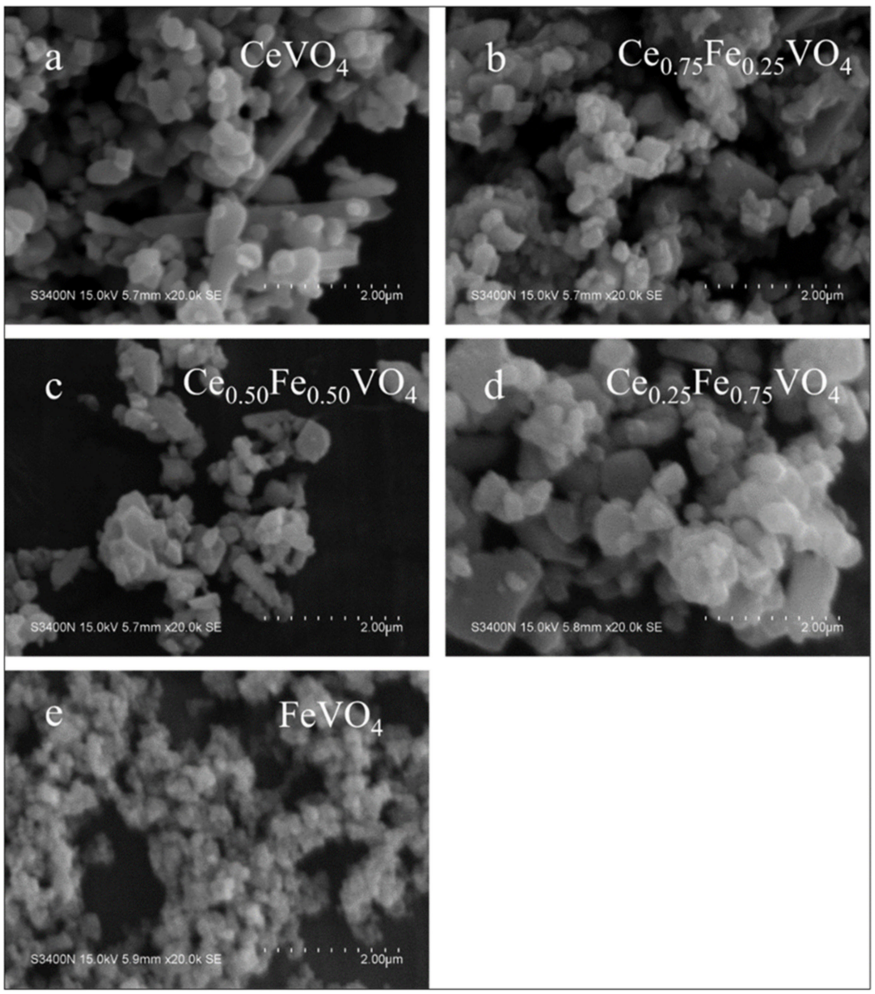

Figure 3. SEM images of $Ce_{1-x}Fe_xVO_4$. (**a**) $CeVO_4$; (**b**) $Ce_{0.75}Fe_{0.25}VO_4$; (**c**) $Ce_{0.50}Fe_{0.50}VO_4$; (**d**) $Ce_{0.25}Fe_{0.75}VO_4$; (**e**) $FeVO_4$.

HRTEM image of $CeVO_4$ is illustrated in Figure 4a. The (200) interplanar spacing is 0.369 nm, equal to that of un-doped $CeVO_4$ (0.369 nm) [34]. The (101) interplanar spacing is 0.484 nm, identical to that of un-doped $CeVO_4$ (0.487 nm) [19,34]. The angle between the (101) and (200) planes (90°) further confirms that the prepared sample is $CeVO_4$. Figure 4b illustrates the HRTEM image of $Ce_{0.50}Fe_{0.50}VO_4$. The d spacing of the (101) plane is 0.482 nm, slightly smaller than that of $CeVO_4$ (0.484 nm). The d spacing of the (200) plane is 0.367 nm, also slightly smaller than that of $CeVO_4$ (0.369 nm). The reason is that the ionic radius of Fe^{3+} (49 pm) is smaller than that of Ce^{3+} (103.8 pm) [32,33]. It is noticeable that the angle between the (101) and (200) planes (101°) is obviously larger than that of $CeVO_4$ (90°). These results mean that some Fe^{3+} substitute the Ce^{4+} and slightly changes the parameters of crystal cells.

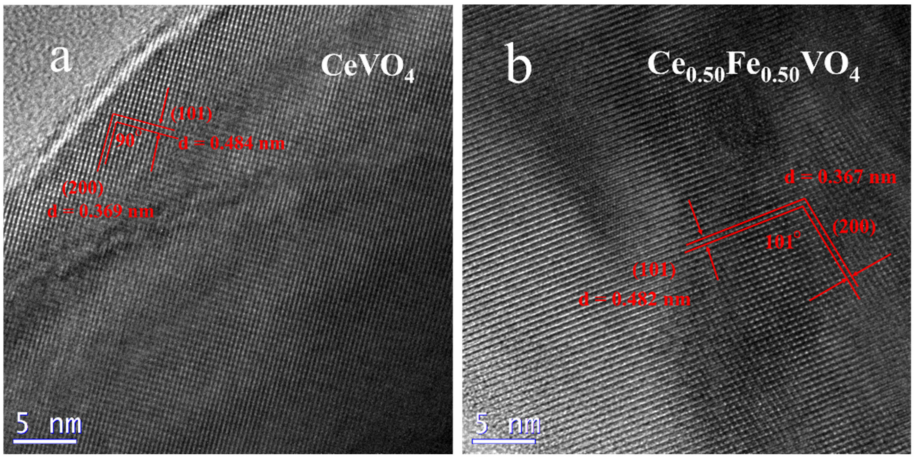

Figure 4. The HRTEM images of $CeVO_4$ (**a**) and $Ce_{0.50}Fe_{0.50}VO_4$ (**b**).

The EDX-mapping data $Ce_{0.50}Fe_{0.50}VO_4$ (Figure 5) show the even distribution of Ce, Fe, V, and O elements. XRF data show that the Ce: Fe: V molar ratio of $Ce_{0.50}Fe_{0.50}VO_4$ is 0.507:0.493:1, close to the theoretical ratio.

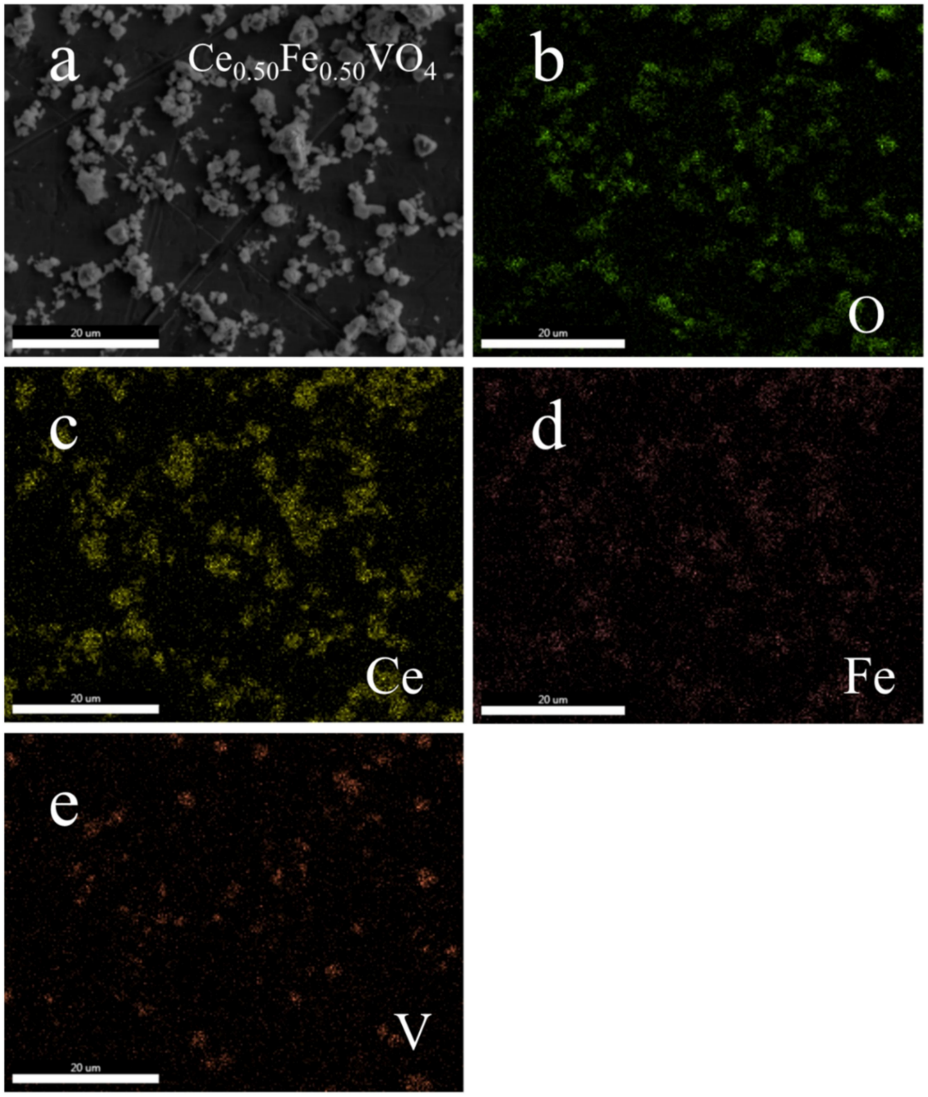

Figure 5. SEM image (**a**) and the corresponding EDX mapping images of O (**b**), Ce (**c**), Fe (**d**) and V (**e**) elements of $Ce_{0.50}Fe_{0.50}VO_4$. The scale bar represents 20 μm.

2.3. XPS Data

Figure 6 gives the Ce 3d XPS spectra. The Ce $3d_{3/2}$ and Ce $3d_{5/2}$ signals are marked as "u" and "v", respectively. The v, v", v"', u, u", and u"' can be ascribed to surface Ce^{4+}, whereas v′ and u′ can be attributed to surface Ce^{3+}. The surface $Ce^{3+}/(Ce^{4+} + Ce^{3+})$ ratio of $CeVO_4$ is 39.1%, corresponding to an average oxidation state (AOS) of 3.61 (for Ce). For comparison, the surface $Ce^{3+}/(Ce^{4+} + Ce^{3+})$ ratio of $Ce_{0.50}Fe_{0.50}VO_4$ is 23.2%, corresponding to an AOS of 3.77.

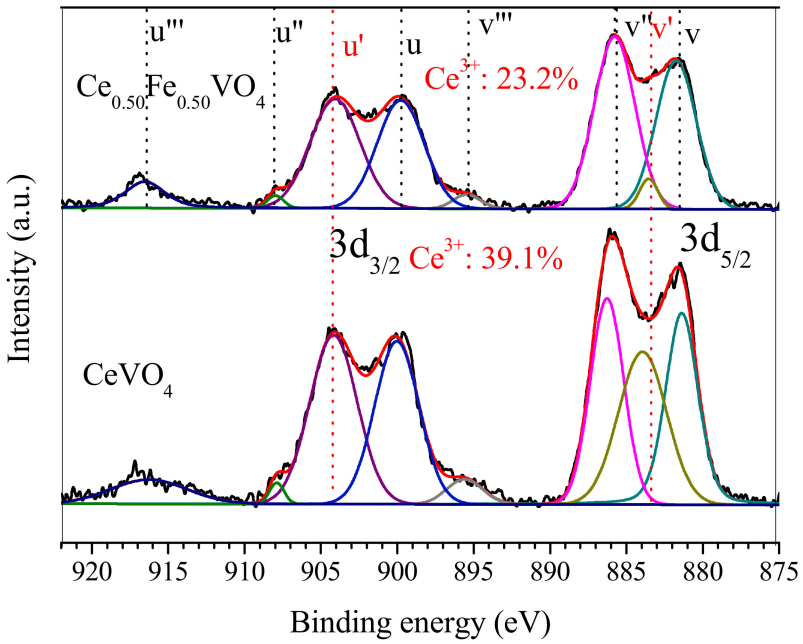

Figure 6. Ce 3d XPS spectra of $CeVO_4$ and $Ce_{0.50}Fe_{0.50}VO_4$.

Figure 7 illustrates the Fe 2p XPS spectra. The surface $Fe^{2+}/(Fe^{2+} + Fe^{3+})$ ratio of $FeVO_4$ is 29.9%, corresponding to an AOS of 2.70 (for Fe). On the other hand, the $Fe^{2+}/(Fe^{2+} + Fe^{3+})$ ratio of $Ce_{0.50}Fe_{0.50}VO_4$ is 28.1%, corresponding to an AOS of 2.72.

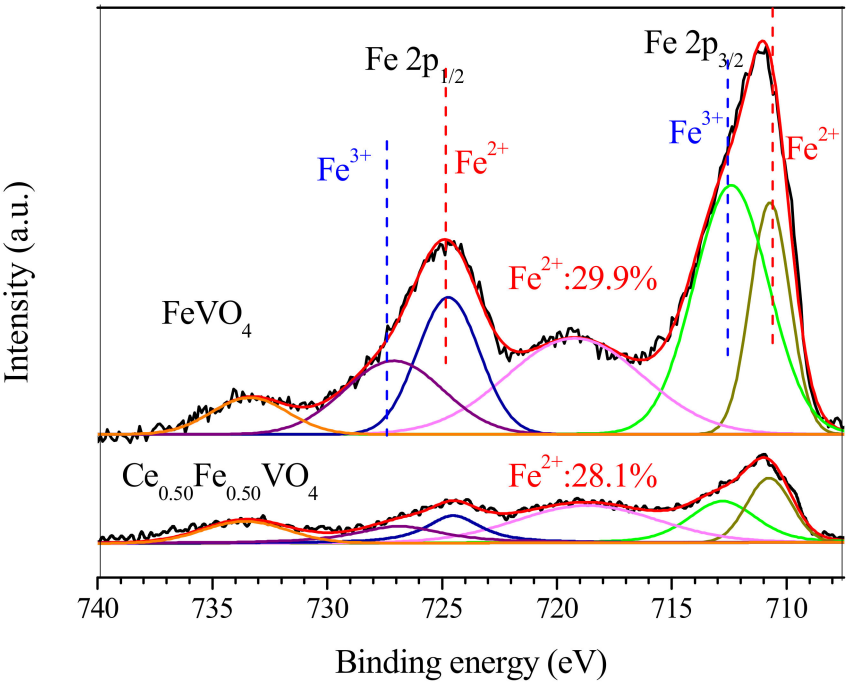

Figure 7. Fe 2p XPS spectra of $CeVO_4$ and $Ce_{0.50}Fe_{0.50}VO_4$.

Figure 8 shows the V 2p XPS spectra. The surface $V^{4+}/(V^{4+} + V^{5+})$ ratio of $Ce_{0.50}Fe_{0.50}VO_4$ is 24.2%, while those of $CeVO_4$ and $FeVO_4$ are 18.7% and 18.9%, respectively, which means the AOSs of V in $Ce_{0.50}Fe_{0.50}VO_4$, $CeVO_4$, and $FeVO_4$ are 4.76, 4.81, 4.81, respectively. The above results manifest that when some Fe^{3+} replace Ce^{4+}, the oxidation states of Fe, Ce, and V are all changed.

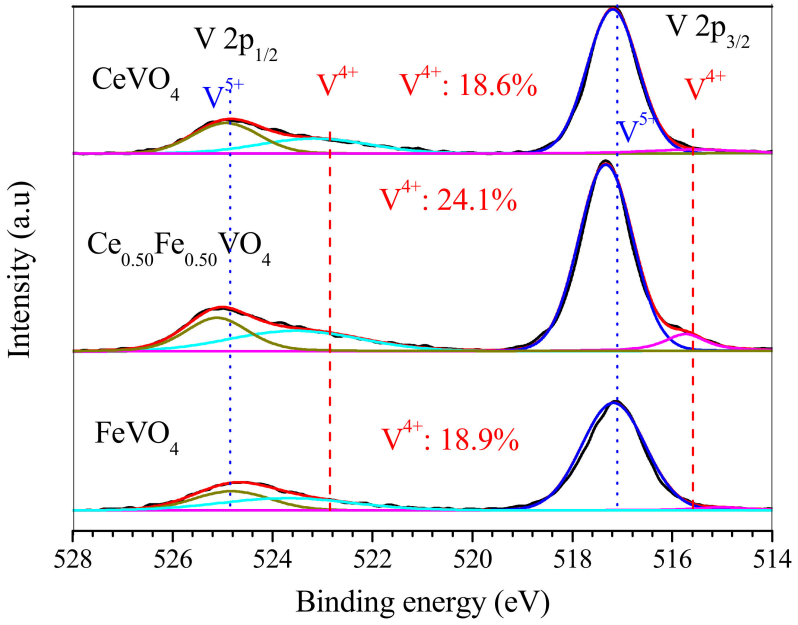

Figure 8. V 2p XPS spectra of $CeVO_4$, $Ce_{0.50}Fe_{0.50}VO_4$, and $FeVO_4$.

Figure 9 shows the O 1s XPS spectra. The O 1s spectra can be divided into two peaks at 529.9, and 531.1 eV corresponding to lattice oxygen (denoted as O_α) as well as the surface oxygen and oxygen vacancies (denoted as O_β), respectively [19,35]. Owing to greater mobility, O_β (surface labile oxygen) is more active compared to O_α (bulk oxygen). As shown in Figure 9, $Ce_{0.5}Fe_{0.5}VO_4$ has the highest concentration of surface labile oxygen species among three representative catalysts.

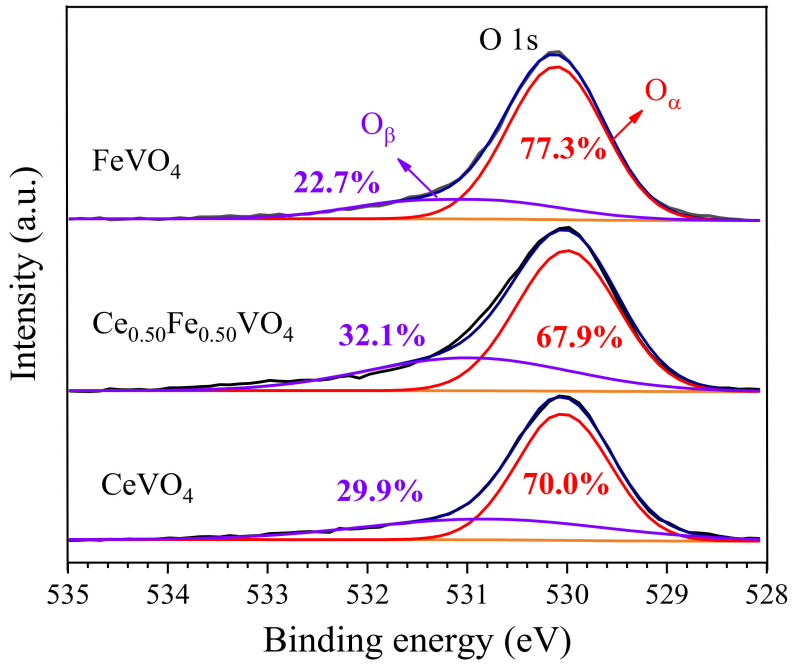

Figure 9. O 1s XPS spectra of $CeVO_4$, $Ce_{0.50}Fe_{0.50}VO_4$, and $FeVO_4$.

2.4. H_2-TPR and NH_3-TPD Data

Figure 10 shows the H_2-TPR profiles of samples. $CeVO_4$ exhibits a peak at 864 °C, corresponding to the reduction of $CeVO_4$ to $CeVO_3$ [24,36]. In the H_2-TPR profile of $FeVO_4$, the obvious peak around 648 °C is assigned to the reduction of VO_4^{3-} [37], while the H_2 consumption at lower temperatures is ascribed to the reduction of Fe^{3+} [16,37]. The first peak of $Ce_{0.50}Fe_{0.50}VO_4$ at 550 °C is ascribed to the reduction of active surface oxygen. The second peak at 632 °C may be ascribed to the reduction of Fe^{3+} or Ce^{4+}. The third peak at 740 °C is ascribed to the reduction of VO_4^{3-} [15,24]. The data show that $Ce_{0.5}Fe_{0.5}VO_4$ owns more surface oxygen useful for NH_3-SCR.

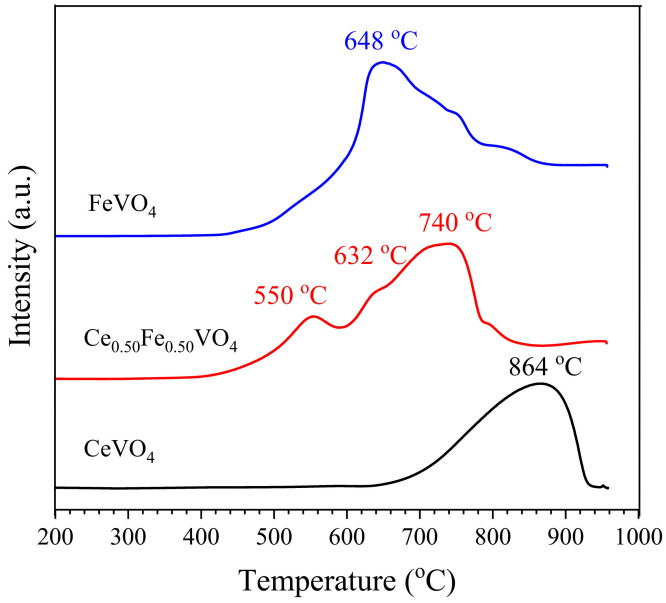

Figure 10. H_2-TPR profiles of the catalysts.

Figure 11 shows the baseline-corrected NH_3-TPD data obtained by subtracting the "blank" TPD profile. The four peaks in low, medium, high, and superhigh temperature regions are ascribed to weak, medium, medium strong, and strong acid sites, as divided by peakfit V4.12 software. The distribution of four kinds of acid sites can be estimated by the relative peak areas. It is observed that the $Fe_{0.50}Ce_{0.50}VO_4$ has more acid sites than $CeVO_4$ and $FeVO_4$, which may be beneficial for NH_3 adsorption and NH_3-SCR [24].

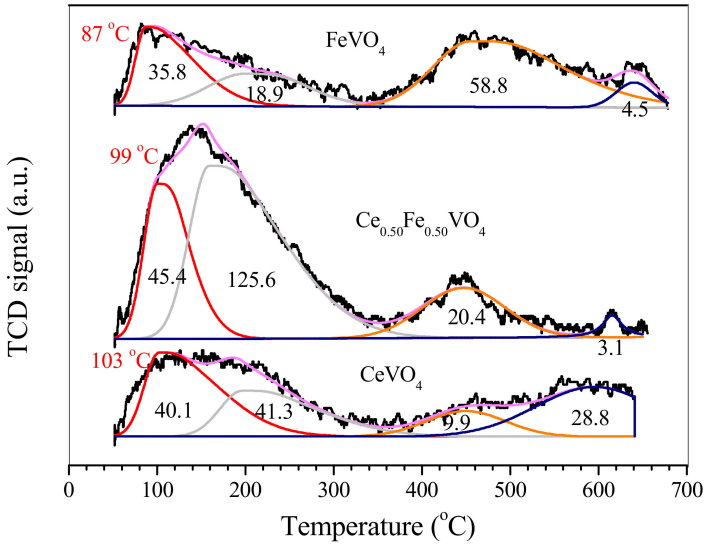

Figure 11. NH_3-TPD profiles of the catalysts.

3. Materials and Methods

3.1. Synthesis

$Ce_{1-x}Fe_xVO_4$ catalysts were synthesized by a modified sol-gel hydrothermal method. In a typical synthesis, 5 mmol NH_4VO_3 was added in 80 mL hot water and heated at 60 °C in a water bath with constant stirring to prepare solution A. Stoichiometric $Fe(NO_3)_3{\cdot}9H_2O$ (98.5% purity, Sinopharm, Shanghai, China), $Ce(NO_3)_3{\cdot}6H_2O$ (99.95%, Aladdin, Beijing, China), and 5 mmol citric acid were separately dissolved in 30 mL ethanol and then these three solutions (about 30 mL each) were mixed and magnetically stirred to form solution B. After 30 min of constant stirring plus heating in a water bath at 60 °C, the solution's color turned from yellowish to transparent and clean. Solution B was added into solution A drop by drop, while the whole solution was stirred vigorously. Subsequently, a moderate amount of propylene oxide was added dropwise into the mixed solution heated in a water bath at 60 °C until a duck-blood-like sol solution was formed. Finally, 2 M $NH_3{\cdot}H_2O$ or 2 M HCl solution was added slowly into the above mixture with constant stirring. The final pH value of the sol solution, monitored by a pH meter, was 7. The sol solution was transferred to two sealed autoclaves (with 100 mL volume each) and hydrothermally treated at 180 °C for 24 h. Then, the solids in the autoclaves were isolated via filtration and washed with deionized water until the pH value of the solvent became 7. The solids were collected and dried at 110 °C for 6 h. The dried solids were carefully grinded in a mortar and transferred into a porcelain bowl and heated to 750 °C (heating rate: 5 °C/min) in a muffle oven (with static air), and then heated at 750 °C for 12 h.

3.2. Activity Measurement

Catalytic activity measurement was performed in a quartz tube reactor (i.d. = 8 mm). The 200 mg catalyst (40–60 mesh) was added in the reactor for each test. The feed gas contained NO (500 ppm), NH_3 (500 ppm), O_2 (3.0%), and balance N_2. The total flow rate was 1000 mL/min. The gas concentrations were measured by an NO–NO_2–NO_x analyzer (42i-HL, High Level, Thermo Electron Corporation, Waltham, MA, USA).

NO_x conversion was calculated using the given equation:

$$X_{NO_x}(\%) = \left(\frac{[NO_x]_{in} - [NO_x]_{out}}{[NO_x]_{in}}\right) \times 100\% \quad (1)$$

where $[NO_x]_{in}$ and $[NO_x]_{out}$ are the concentrating of NO_x entering the reactor and exiting the reactor, respectively.

3.3. Characterization

XRD patterns were recorded on an Advanced D8 (Bruker) powder diffractometer using Cu K_α radiation. TEM images were obtained with a JEOL JEM-2100F field emission TEM instrument equipped with an EDAX Genesis XM4-Sys60 system (EDAX Inc., Mahwah, NJ, USA). The elemental compositions of powders were determined by XRF (Thermo-3600, Thermo Fisher Scientific Inc., Waltham, MA, USA). The specific BET surface data were measured using a Micromeritics analyzer (Tristar II 3020M, Micromeritics, Norcross, GA, USA). XPS data were obtained on a thermoESCLAB 250XI instrument using monochromatic Al Kα radiation (Thermo, Waltham, MA, USA).

H_2-TPR experiments were carried out using a Micromeritics AutoChem 2920 (Micromeritics, Norcross, GA, USA) chemisorption instrument, following the procedure reported [38,39]. Firstly, the sample (40–60 mesh, 100 mg) was placed in a quartz tube reactor. Secondly, the sample was pretreated at 300 °C in 20 vol.% O_2/Ar (50 mL/min) for 0.5 h and cooled down to 30 °C followed by purging by Ar for 0.5 h. Then, a gas flow (10% H_2 in Ar, 50 mL/min) passed through the sample. Finally, the temperature was increased from 50 to 950 °C at a rate of 10 °C min^{-1}.

NH_3-TPD experiments were carried out on a Micromeritics AutoChem 2920 chemisorption instrument. A sample (40–60 mesh, 50 mg), placed in a quartz reactor, was pretreated

at 300 °C in 20 vol.% O_2/Ar (50 mL/min) for 0.5 h and cooled down to 30 °C followed by Ar purging for 0.5 h. Then, 10% NH_3 in Ar (50 mL/min) flowed through the sample, and the temperature was ramped from 50 to 650 °C at a rate of 10 °C min^{-1}.

4. Conclusions

A series of $Ce_{1-x}Fe_xVO_4$ catalysts were prepared by a modified hydrothermal method. It was found that that $Ce_{0.50}Fe_{0.50}VO_4$ exhibits the optimum NO_x conversion efficiency compared with other catalysts. With the incorporation of Fe^{3+}, the crystal structure of $CeVO_4$ crystal gradually distorts and the average oxidation states of Ce, Fe, and V change accordingly. The surface oxygen and oxygen vacancy contents increase, as proved by XPS and H_2-TPR data. $Ce_{0.50}Fe_{0.50}VO_4$ has more weak and medium acid sites compared with $CeVO_4$ and $FeVO_4$. These factors contribute to the enhanced catalytic performance of $Ce_{0.50}Fe_{0.50}VO_4$. The anti-SO_2 and anti-H_2O performance of NH_3-SCR catalysts should be studied in the future for applications under realistic environments.

Supplementary Materials: The following supporting information can be downloaded at: https://www.mdpi.com/article/10.3390/catal12050549/s1, Table S1. The crystallographic data of $Ce_{1-x}Fe_xVO_4$ samples, some of which were obtained using the Rietveld refinements. Figure S1. X_{NOx} over $Ce_{1-x}Fe_xVO_4$ catalysts prepared by a hydrothermal method. Reaction conditions: [NO] = 500 ppm, [NH_3] = 500 ppm, [O_2] = 3 vol.%, balance N_2; catalyst weight: 200 mg; total flow rate: 1000 mL·min^{-1}. Figure S2. X_{NOx} over $Ce_{0.5}Fe_{0.5}VO_4$ at 300 °C as a function of time on stream. Reaction conditions: [NO] = 500 ppm, [NH_3] = 500 ppm, [O_2] = 3 vol.%, balance N_2; catalyst weight: 200 mg; total flow rate: 1000 mL·min^{-1}. Figure S3. XRD patterns (2θ = 22–27°) of $Ce_{1-x}Fe_xVO_4$ catalysts.

Author Contributions: Conceptualization, J.W.; Data curation, J.W. and X.Z.; Formal analysis, L.W. and H.C.; Investigation, L.W. and X.Z.; Supervision, Z.M.; Writing—original draft, L.W. and J.W.; Writing—review and editing, Z.M. All authors have read and agreed to the published version of the manuscript.

Funding: This work was financially supported by the Natural Science Research Key Project of Anhui Provincial Department of Education (KJ2021A1036), Natural Science Foundation of Zhejiang province (Y5090310, LY19E080023), Natural Science Foundation of Anhui province (KJ2018A0406), the Open Foundation of State Key Laboratory of Precision Spectroscopy (East China Normal University), Excellent and top-notch talent cultivation funding project in Anhui universities (GXFX2017106), and Special Fund for the Construction of Innovative Provinces (2020XZX005).

Data Availability Statement: Data are available from the authors.

Conflicts of Interest: The authors declare no conflict of interest.

References

1. Jiang, Y.; Bao, C.Z.; Liu, Q.Y.; Liang, G.T.; Lu, M.Y.; Ma, S.Y. A novel CeO_2-MoO_3-WO_3/TiO_2 catalyst for selective catalytic reduction of NO with NH_3. *Catal. Commun.* **2018**, *103*, 96–100. [CrossRef]
2. Wang, D.; Chen, Q.Z.; Zhang, X.; Gao, C.; Wang, B.; Huang, X.; Peng, Y.; Li, J.H.; Lu, C.M.; Crittenden, J. Multipollutant control (MPC) of flue gas from stationary sources using SCR technology: A critical review. *Environ. Sci. Technol.* **2021**, *55*, 2743–2766. [CrossRef] [PubMed]
3. Xu, G.Y.; Guo, X.L.; Cheng, X.X.; Yu, J.; Fang, B.Z. A review of Mn-based catalysts for low-temperature NH_3-SCR: NO_x removal and H_2O/SO_2 resistance. *Nanoscale* **2021**, *13*, 7052–7080. [CrossRef] [PubMed]
4. Duan, C.P.; Guo, R.T.; Wu, G.L.; Pan, W.G. Selective catalytic reduction of NO_x by NH_3 over $CeVO_4$-CeO_2 nanocomposite. *Environ. Sci. Pollut. Res.* **2020**, *27*, 22818–22828. [CrossRef]
5. Zhang, W.D.; Qi, S.H.; Pantaleo, G.; Liotta, L.F. WO_3–V_2O_5 active oxides for NO_x SCR by NH_3: Preparation methods, catalysts' composition, and deactivation mechanism—A review. *Catalysts* **2019**, *9*, 527. [CrossRef]
6. Gao, F.Y.; Tang, X.L.; Yi, H.H.; Li, J.Y.; Zhao, S.Z.; Wang, J.G.; Chu, C.; Li, C.L. Promotional mechanisms of activity and SO_2 tolerance of Co- or Ni-doped MnO_x-CeO_2 catalysts for SCR of NO_x with NH_3 at low temperature. *Chem. Eng. J.* **2017**, *317*, 20–31. [CrossRef]
7. Wu, Z.H.; Zeng, Y.Q.; Song, F.J.; Zhang, S.L.; Zhong, Q. Active sites assembly effect on CeO_2-WO_3-TiO_2 catalysts for selective catalytic reduction of NO with NH_3. *Mol. Catal.* **2019**, *479*, 110549. [CrossRef]

8. Song, Z.X.; Yin, L.T.; Zhang, Q.L.; Ning, P.; Duan, Y.K.; Wang, J.; Liu, X.; Long, K.X.; Huang, Z.Z. Relationship between the WO_3 states and reaction pathway over CeO_2-ZrO_2-WO_3 catalysts for selective catalytic reduction of NO with NH_3. *Mol. Catal.* **2017**, *437*, 95–104. [CrossRef]
9. Shen, B.X.; Zhang, X.P.; Ma, H.Q.; Yao, Y.; Liu, T. A comparative study of Mn/CeO_2, Mn/ZrO_2 and Mn/Ce-ZrO_2 for low temperature selective catalytic reduction of NO with NH_3 in the presence of SO_2 and H_2O. *J. Environ. Sci.* **2013**, *25*, 791–800. [CrossRef]
10. Liu, C.; Gao, G.; Shi, J.W.; He, C.; Li, G.D.; Bai, N.; Niu, C. MnO_x-CeO_2 shell-in-shell microspheres for NH_3-SCR de-NO_x at low temperature. *Catal. Commun.* **2016**, *86*, 36–40. [CrossRef]
11. Chang, H.Z.; Chen, X.Y.; Li, J.H.; Ma, L.; Wang, C.Z.; Liu, C.X.; Schwank, J.W.; Hao, J.M. Improvement of activity and SO_2 tolerance of Sn-modified MnO_x-CeO_2 catalysts for NH_3-SCR at low temperatures. *Environ. Sci. Technol.* **2013**, *47*, 5294–5301. [CrossRef] [PubMed]
12. Jiang, H.X.; Zhao, J.; Jiang, D.Y.; Zhang, M.H. Hollow MnO_x-CeO_2 nanospheres prepared by a green route: A novel low-temperature NH_3-SCR catalyst. *Catal. Lett.* **2014**, *144*, 325–332. [CrossRef]
13. Peng, Y.; Li, J.H.; Huang, X.; Li, X.; Su, W.K.; Sun, X.X.; Wang, D.Z.; Hao, J.M. Deactivation mechanism of potassium on the V_2O_5/CeO_2 catalysts for SCR reaction: Acidity, reducibility and adsorbed-NO_x. *Environ. Sci. Technol.* **2014**, *48*, 4515–4520. [CrossRef] [PubMed]
14. Kang, L.; Han, L.P.; Wang, P.L.; Feng, C.; Zhang, J.P.; Yan, T.T.; Deng, J.; Shi, L.Y.; Zhang, D.S. SO_2-tolerant NO_x reduction by marvelously suppressing SO_2 adsorption over $Fe_\delta Ce_{1-\delta}VO_4$ catalysts. *Environ. Sci. Technol.* **2020**, *54*, 14066–14075. [CrossRef]
15. Wu, G.X.; Li, J.; Fang, Z.T.; Lan, L.; Wang, R.; Gong, M.C.; Chen, Y.Q. $FeVO_4$ nanorods supported TiO_2 as a superior catalyst for NH_3–SCR reaction in a broad temperature range. *Catal. Commun.* **2015**, *64*, 75–79. [CrossRef]
16. Wu, G.X.; Feng, X.; Zhang, H.L.; Zhang, Y.H.; Wang, J.L.; Chen, Y.Q.; Dan, Y. The promotional role of Ni in $FeVO_4/TiO_2$ monolith catalyst for selective catalytic reduction of NO with NH_3. *Appl. Surf. Sci.* **2018**, *427*, 24–36. [CrossRef]
17. Casanova, M.; Llorca, J.; Sagar, A.; Schermanz, K.; Trovarelli, A. Mixed iron–erbium vanadate NH_3-SCR catalysts. *Catal. Today* **2015**, *241*, 159–168. [CrossRef]
18. Huang, X.S.; Zhang, G.D.; Dong, F.; Tang, Z.C. The remarkable promotional effect of Sn on $CeVO_4$ catalyst for wide temperature NH_3-SCR process by citric acid-assisted solvothermal synthesis and post-hydrothermal treatment. *Catal. Sci. Technol.* **2018**, *8*, 5604–5615. [CrossRef]
19. Wu, G.L.; Guo, R.T.; Liu, Y.Z.; Duan, C.P.; Miao, Y.F.; Gu, J.W.; Pan, W.G. Promoting effect of Sb on the selective catalytic reduction of NO with NH_3 over $CeVO_4$ catalyst. *J. Energy Inst.* **2021**, *95*, 77–86. [CrossRef]
20. Kim, J.; Kim, D.H.; Kwon, D.W.; Lee, K.Y.; Ha, H.P. Unveiling the traits of rare earth metal (RM)-substituted bimetallic $Ce_{0.5}RM_{0.5}V_1O_4$ phases to activate selective NH_3 oxidation and NO_X reduction. *Appl. Surf. Sci.* **2020**, *518*, 146238. [CrossRef]
21. Casanova, M.; Schermanz, K.; Llorca, J.; Trovarelli, A. Improved high temperature stability of NH_3-SCR catalysts based on rare earth vanadates supported on TiO_2-WO_3-SiO_2. *Catal. Today* **2012**, *184*, 227–236. [CrossRef]
22. Gillot, S.; Tricot, G.; Vezin, H.; Dacquin, J.P.; Dujardin, C.; Granger, P. Induced effect of tungsten incorporation on the catalytic properties of $CeVO_4$ systems for the selective reduction of NO_x by ammonia. *Appl. Catal. B Environ.* **2018**, *234*, 318–328. [CrossRef]
23. Zhao, X.; Huang, L.; Namuangruk, S.; Hu, H.; Hu, X.N.; Shi, L.Y.; Zhang, D.S. Morphology-dependent performance of Zr-$CeVO_4/TiO_2$ for selective catalytic reduction of NO with NH_3. *Catal. Sci. Technol.* **2016**, *6*, 5543–5553. [CrossRef]
24. Zhao, X.; Huang, L.; Li, H.R.; Hu, H.; Hu, X.N.; Shi, L.Y.; Zhang, D.S. Promotional effects of zirconium doped $CeVO_4$ for the low-temperature selective catalytic reduction of NO_x with NH_3. *Appl. Catal. B Environ.* **2016**, *183*, 269–281. [CrossRef]
25. Si, Z.P.; Shen, Y.J.; He, J.B.; Yan, T.T.; Zhang, J.P.; Deng, J.; Zhang, D.S. SO_2-induced alkali resistance of $FeVO_4/TiO_2$ catalysts for NO_x reduction. *Environ. Sci. Technol.* **2022**, *56*, 605–613. [CrossRef] [PubMed]
26. Damma, D.; Ettireddy, P.R.; Reddy, B.M.; Smirniotis, P.G. A review of low temperature NH_3-SCR for removal of NO_x. *Catalysts* **2019**, *9*, 349. [CrossRef]
27. Wang, L.; Wang, J.B.; Liu, X.N.; Chen, Y.X.; Cheng, H.P.; Wu, Y.B.; Peng, H.; Ma, Z. $FeCeO_x$ with improved activity for catalytic reduction of NO with NH_3. *J. Phys. Chem. Solids* **2020**, *142*, 109472. [CrossRef]
28. Guan, J.; Li, J.; Ye, Z.; Wu, D.; Liu, C.; Wang, H.; Ma, C.; Huo, P.; Yan, Y. La_2O_3 media enhanced electrons transfer for improved $CeVO_4$@halloysite nanotubes photocatalytic activity for removing tetracycline. *J. Taiwan Inst. Chem. Eng.* **2019**, *96*, 281–298. [CrossRef]
29. Hu, X.L.; Qu, W.Y.; Chen, J.X.; Xu, D.R.; Liu, J.; Dong, Y.Y.; Liu, R.; Ma, Z.; Tang, X.F. Speeding up low-temperature SCR with reactants-coupling dual catalytic sites. *Chem. Eng. J.* **2022**, *440*, 135832. [CrossRef]
30. Lu, G.; Song, B.; Li, Z.; Liang, H.Y.; Zou, X.J. Photocatalytic degradation of naphthalene on $CeVO_4$ nanoparticles under visible light. *Chem. Eng. J.* **2020**, *402*, 125645. [CrossRef]
31. Lopez-Moreno, S.; Errandonea, D.; Pellicer-Porres, J.; Martinez-Garcia, D.; Patwe, S.J.; Achary, S.N.; Tyagi, A.K.; Rodriguez-Hernandez, P.; Munoz, A.; Popescu, C. Stability of $FeVO_4$ under pressure: An X-ray diffraction and first-principles study. *Inorg. Chem.* **2018**, *57*, 7860–7876. [CrossRef] [PubMed]
32. Anjaneya, K.C.; Nayaka, G.P.; Manjanna, J.; Govindaraj, G.; Ganesha, K.N. Studies on structural, morphological and electrical properties of $Ce_{0.8}Ln_{0.2}O_{2-x}$ (Ln = Y^{3+}, Gd^{3+}, Sm^{3+}, Nd^{3+} and La^{3+}) solid solutions prepared by citrate complexation method. *J. Alloy. Compd.* **2014**, *585*, 594–601. [CrossRef]

33. Qu, W.Y.; Chen, Y.X.; Huang, Z.W.; Gao, J.Y.; Zhou, M.J.; Chen, J.X.; Li, C.; Ma, Z.; Chen, J.M.; Tang, X.F. Active tetrahedral iron sites of γ-Fe_2O_3 catalyzing NO reduction by NH_3. *Environ. Sci. Technol. Lett.* **2017**, *4*, 246–250. [CrossRef]
34. Yao, L.; Li, X.; Liu, H.; Li, Z.; Lu, Q. One-dimensional hierarchical $CeVO_4/TiO_2$ heterostructures with enhanced photocatalytic performance. *J. Nanopart. Res.* **2019**, *21*, 140. [CrossRef]
35. Wang, Y.; Liu, H.; Hu, P.P.; Huang, Z.W.; Gao, J.Y.; Xu, F.; Ma, Z.; Tang, X.F. Enhancing the catalytic activity of hollandite manganese oxide by supporting sub-10 nm ceria particles. *Catal. Lett.* **2015**, *145*, 1880–1884. [CrossRef]
36. Gillot, S.; Tricot, G.; Vezin, H.; Dacquin, J.P.; Dujardin, C.; Granger, P. Development of stable and efficient $CeVO_4$ systems for the selective reduction of NO_x by ammonia: Structure-activity relationship. *Appl. Catal. B Environ.* **2017**, *218*, 338–348. [CrossRef]
37. Wu, G.; Li, J.; Fang, Z.; Lan, L.; Wang, R.; Lin, T.; Gong, M.; Chen, Y. Effectively enhance catalytic performance by adjusting pH during the synthesis of active components over $FeVO_4/TiO_2$–WO_3–SiO_2 monolith catalysts. *Chem. Eng. J.* **2015**, *271*, 1–13. [CrossRef]
38. Lian, Z.H.; Liu, F.D.; He, H. Enhanced activity of Ti-modified V_2O_5/CeO_2 catalyst for the selective catalytic reduction of NO_x with NH_3. *Ind. Eng. Chem. Res.* **2014**, *53*, 19506–19511. [CrossRef]
39. Chen, Y.X.; Huang, Z.W.; Hu, P.P.; Chen, J.M.; Tang, X.F. Improved performance of supported single-atom catalysts via increased surface active sites. *Catal. Commun.* **2016**, *75*, 74–77. [CrossRef]